Supporting Information

Electronic modulation of a single-atom-based tandem catalyst boosts CO$_2$ photoreduction to ethanol

Shuaiqi Gong[a], Baoxin Ni[d], Xiaoyang He[a], Jianying Wang[a], Kun Jiang[d], Deli Wu[c],

Yulin Min[b], Hexing Li[b,*], Zuofeng Chen[a,*]

[a]School of Chemical Science and Engineering, Tongji University, 1239 Siping Road,

Shanghai 200092, China;

[b]Shanghai Key Laboratory of Materials Protection and Advanced Materials in Electric

Power, Shanghai University of Electric Power, Shanghai 200090, China;

[c]State Key Laboratory of Pollution Control and Resources Reuse, College of

Environmental Science & Engineering, Tongji University, Shanghai 200092, China;

[d]Interdisciplinary Research Center, School of Mechanical Engineering, Shanghai Jiao

Tong University, Shanghai 200240, China.

*zfchen@tongji.edu.cn (Z.-F. C.)

Experimental section

Chemicals

Copper (II) chloride (CuCl$_2$, 98%), indium (III) nitrate hydrate (In(NO$_3$)$_3$·4H$_2$O,

99.99%), *p*-terephthalic acid (PTA, 99%) and N,N-dimethylformamide (DMF, 99.5%)

were purchased from Shanghai Aladdin Regent Co., Ltd., China. α-terpineol (98%),

sodium sulfate anhydrous (Na$_2$SO$_4$, 99%), and ethyl cellulose were purchased from

MACKLIN Reagent Co., Ltd. All reagents were used as received without further purification.

Characterizations

Scanning electron microscopy (SEM) and transmission electron microscopy (TEM) were conducted using the Hitachi S-4800 and FEI talos F200x G2 instruments, respectively, to analyze the morphologies of the materials. Elemental mapping was performed using energy dispersive X-ray spectroscopy (EDX) with Super-x analysis. Spherical aberration-corrected scanning TEM (AC-STEM, EM-ARM300F) and X-ray absorption spectroscopy (XAS) were employed for the analysis of single atoms. The absorption coefficient data in the XANES region were obtained by applying consistent procedures for pre-edge line fitting, post-edge curve fitting, and edge-step normalization across all the data. The XANES and EXAFS data processing and analysis were carried out using the IINFFIT package.[1] X-ray powder diffraction (XRD) measurements were performed on the D8 Advanced X-ray diffractometer (Burker - AXS D8 Advance, 2014) with Cu Kα radiation. X-ray photoelectron spectroscopy (XPS) and Auger electron spectroscopy (AES) measurements were conducted using the Kratos Axis UltraDLD instrument with Al Kα X-ray (1486.6 eV) radiation. FT-IR spectra of powder samples were recorded on a Nicolet 6700 spectrometer (Thermo Fisher Nicolet, USA) using KBr pellets. Raman spectra were obtained using a Raman spectrometer from Thermo Scientific with a 532 nm laser source. UV-Vis-NIR diffused reflectance spectra (DRS) were collected on a spectrophotometer (UV-3100, Shimadzu,

Japan) with $BaSO_4$ as the background holder. Photoluminescence (PL) and time-resolved PL (TRPL) spectra were acquired at room temperature using FLUOROLOG-3-11. The photoelectrochemical measurements were carried out on a CHI 760E electrochemical workstation (Chenhua, Shanghai). CO_2 temperature-programmed desorption (TPD) measurements were performed using a Quantachrome Autosorb-iQC chemisorption analyzer with a thermal conductivity detector. N_2 and CO_2 adsorption isotherms were obtained using an ASAP2020M apparatus. The samples were degassed in vacuum at 120 °C for 6 hours and then measured at -196 °C for N_2 adsorption and at 25 °C for CO_2 adsorption. Photocatalytic experiments were conducted with a 300 W Xe lamp (PerfectLight, Beijing) as the light source coupled with a UVCUT-420 nm filter. The gases produced from the CO_2 photoreduction system were analyzed and quantified using an online gas chromatography (GC) system (GC-2014, Shimadzu) equipped with a thermal conductivity detector (TCD) and two flame-ionized detectors (FIDs). The origin of photocatalytic CO_2 reduction products was determined using isotope-labeled $^{13}CO_2$ (99%) and analyzed by gas chromatography-mass spectrometry (GC-MS) (Trace 1310 GC-ISQ quadrupole MS, ThermoFisher, USA). Liquid products obtained at the end of photocatalysis were analyzed by ^1H nuclear magnetic resonance (NMR) using an AVANCE III HD 600 MHz instrument.

Methods

Synthesis of In-MOF prism. The synthesis of the In-MOF was carried out following our previous work.[2] In a typical procedure, 60 mg of $In(NO_3)_3 \cdot 4H_2O$ and 60

mg of PTA were added to 40 mL of DMF and vigorously stirred at 120 °C for 30 minutes.

Synthesis of InCu-MOF caterpillar-like prism. The obtained In-MOF (8 mg) was transferred to 4 mL of anhydrous ethanol and subjected to strong ultrasound. Subsequently, 4 mL of a 0.025 mM $CuCl_2$ solution was added dropwise to the In-MOF ethanol suspension with stirring. The stirring time was strictly controlled, with the InCu-MOF (Cu-O_3) and InCu-MOF (Cu-O_4) precursors stirred for 2 and 5 minutes, respectively. The as-prepared InCu-MOF was immediately collected by centrifugation, followed by washing with ethanol and vacuum drying overnight.

Synthesis of In_2O_3/Cu-O_x (x = 3 and 4) porous hollow microtubes. The obtained InCu-MOF (Cu-O_3) and InCu-MOF (Cu-O_4) precursors were annealed in air at 500 °C for 2 hours with a ramp rate of 1 °C/min to obtain In_2O_3/Cu-O_3 and In_2O_3/Cu-O_4, respectively.

Synthesis of Cu-MOF. The synthesis of Cu-MOF followed the same procedure as that of InCu-MOF, except that the stirring time was extended to 10 minutes.

Synthesis of CuO. The obtained Cu-MOF precursors were annealed in air at 500 °C for 2 hours with a ramp rate of 1 °C/min.

Photocatalytic CO_2 reduction measurements. The photocatalytic CO_2 reduction measurements of all samples were conducted using an online trace gas analysis system (Labsolar 6A, PerfectLight). In detail, 10 mg of catalysts and 10 mL of distilled water were added to a Pyrex glass reaction cell, which was then filled with CO_2 and sonicated. The photocatalytic CO_2RR was performed under visible light irradiation ($\lambda > 420$ nm).

The produced products were analyzed by GC and ^{1}H NMR every hour. For the ^{1}H NMR measurement, 0.5 mL of the product solution was mixed with 0.1 mL of D_2O and 10 µL of dimethylsulfoxide (DMSO, used as the internal standard).

Photoelectrochemical measurements. The ink composition consisted of 7 mg of photocatalysts, 2 mL of ethanol, 1 mL of α-terpineol, and 1 mg of ethyl cellulose. The ink was coated on fluorine-doped tin oxide (FTO) conductive glasses (1 cm × 1 cm) as the working electrode. The photoelectrochemical measurements were conducted in a three-electrode configuration system on a CHI 760A electrochemical workstation, with a Pt plate as the counter electrode and Ag/AgCl as the reference electrode. The photocurrent was measured in a 0.5 M Na_2SO_4 solution. Electrochemical impedance spectroscopy (EIS) and linear sweep voltammetry (LSV) measurements were carried out in CO_2-saturated 0.5 M $KHCO_3$ solution.

AQE tests. The apparent quantum efficiency (AQE) for ethanol production was measured with 420 ± 20 nm band pass filter and calculated by the following equation:

$$AQE\ (\%) = \frac{number\ of\ the\ elections\ taking\ part\ in\ reduction}{number\ of\ incident\ photons} \times 100\%$$

where n (CH_3CH_2OH) is the number of CH_3CH_2OH molecules produced and I represents the number of incident photons.

In situ DRIFTS tests. In situ DRIFTS spectra were recorded to detect the intermediates during the CO_2 reduction process. The measurements were performed using a Thermofisher IS50 spectrometer equipped with Harrick accessories. The

reaction chamber was purged with Ar gas and then filled with CO_2. The spectra were collected periodically under visible light irradiation. Each spectrum was recorded by averaging 20 scans at a 4 cm^{-1} spectral resolution.

In situ Raman tests. The ink used for in situ Raman analysis contained 10 mg of photocatalysts, 500 μL H_2O, 460 μL isopropanol, and 40 μL Nafion. The ink was coated on a sample cell (type-K004, Tianjin Aida) equipped with a 3 mm thick quartz window and a 5 mm × 5 mm gold plate. The sample cell was purged with Ar gas and then filled with CO_2. In situ Raman spectra were recorded using a LabRAM HR Evolution (Horiba) instrument with a 633 nm laser. The irradiation device employed an optical fiber.

Computational method. All spin-polarized density functional theory (DFT) calculations were performed using the Vienna Ab initio Simulation Package (VASP) software.[3, 4] The projector augmented plane wave (PAW) pseudopotential and the Perdew–Burke–Ernzerhof generalized gradient approximation (PBE-GGA) exchange-correlation functional were used to describe the ionic cores.[5, 6] A plane-wave expansion for the basis set was employed with a cutoff energy of 500 eV. The total energy convergence criterion was set to 10^{-5} eV, and the force convergence criterion on each atom was set to 0.02 eV/Å. The slab model included a vacuum layer of 15 Å to separate the slabs along the perpendicular Z-direction. The adsorption energy was calculated as ΔE_{abs} ($\Delta E_{abs} = E_{(slab\text{-}abs)} - E_{(slab)} - E_{(abs)}$).
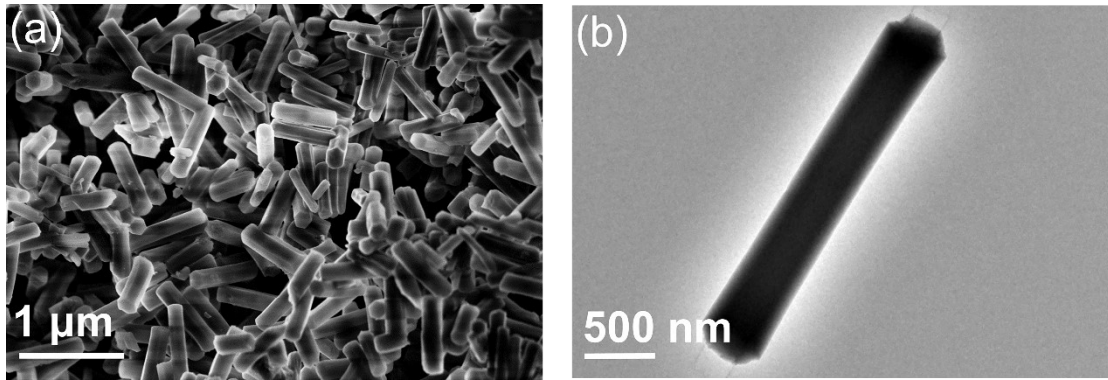
Figure S1. (a) SEM and (b) TEM images of In-MOF.
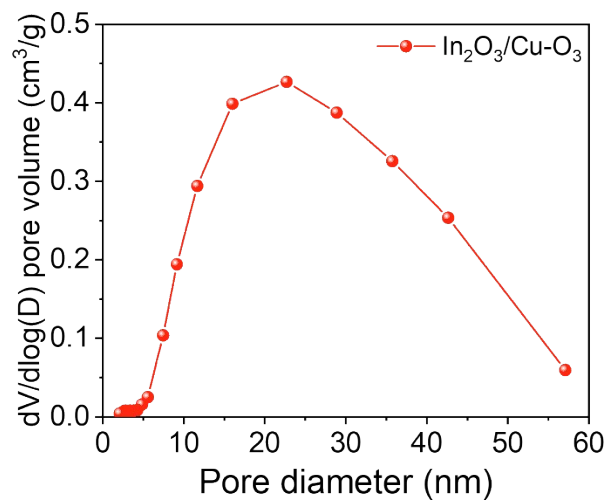
Figure S2. The pore size distribution curve of $In_2O_3/Cu-O_3$.
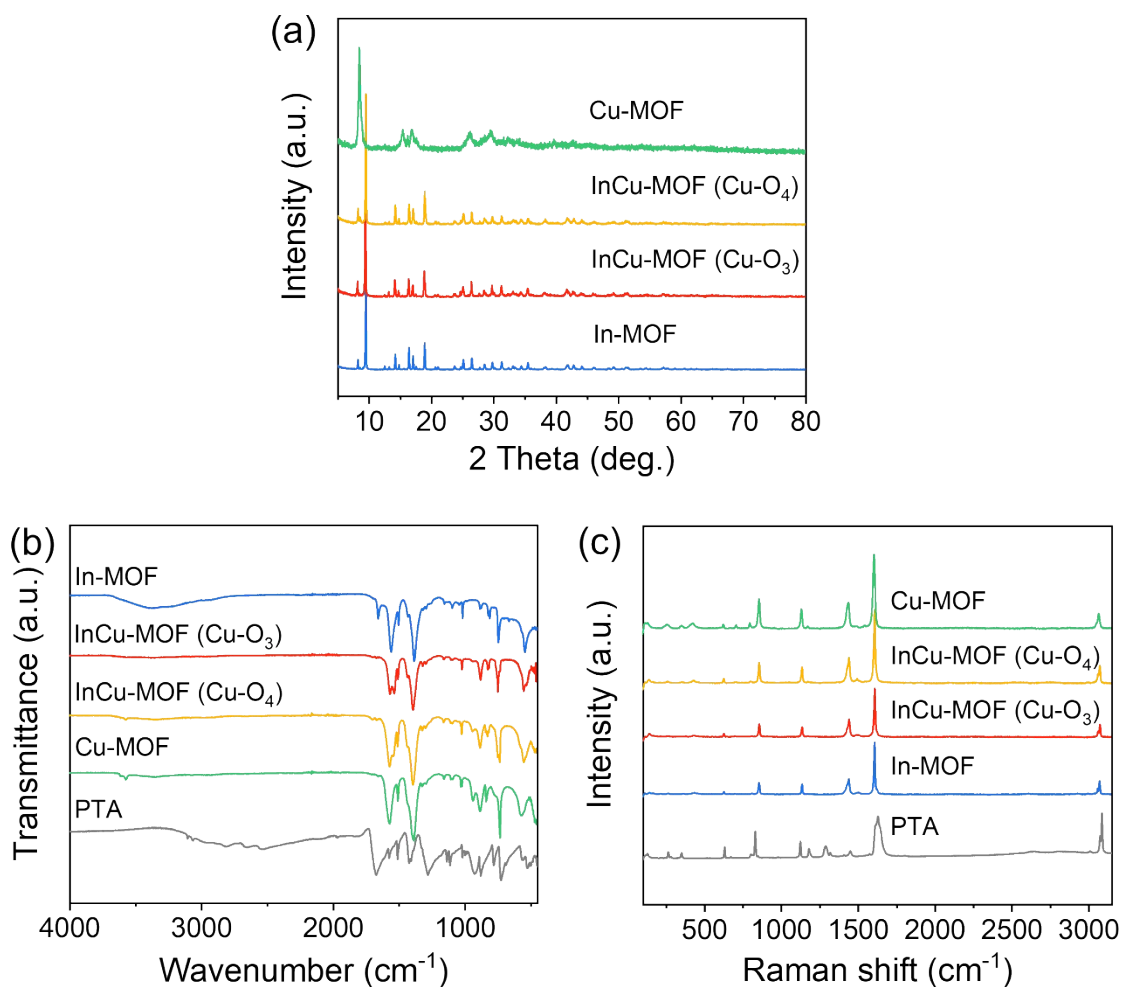
Figure S3. (a) XRD patterns of In-MOF, InCu-MOF (Cu-O$_3$ and Cu-O$_4$) and Cu-MOF.

(b) FT-IR and (c) Raman spectra of In-MOF, InCu-MOF (Cu-O$_3$ and Cu-O$_4$), Cu-MOF

and PTA.
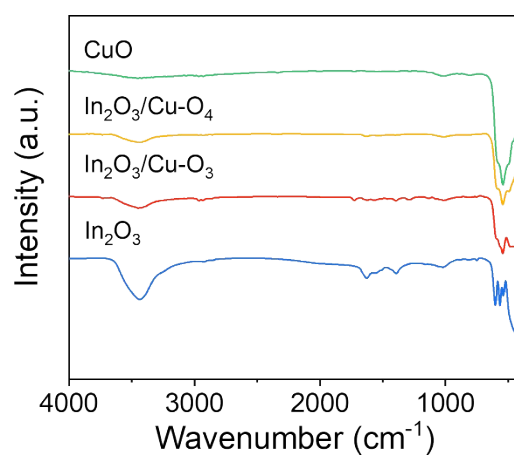
Figure S4. FT-IR spectra of In$_2$O$_3$, In$_2$O$_3$/Cu-O$_3$, In$_2$O$_3$/Cu-O$_4$ and CuO.
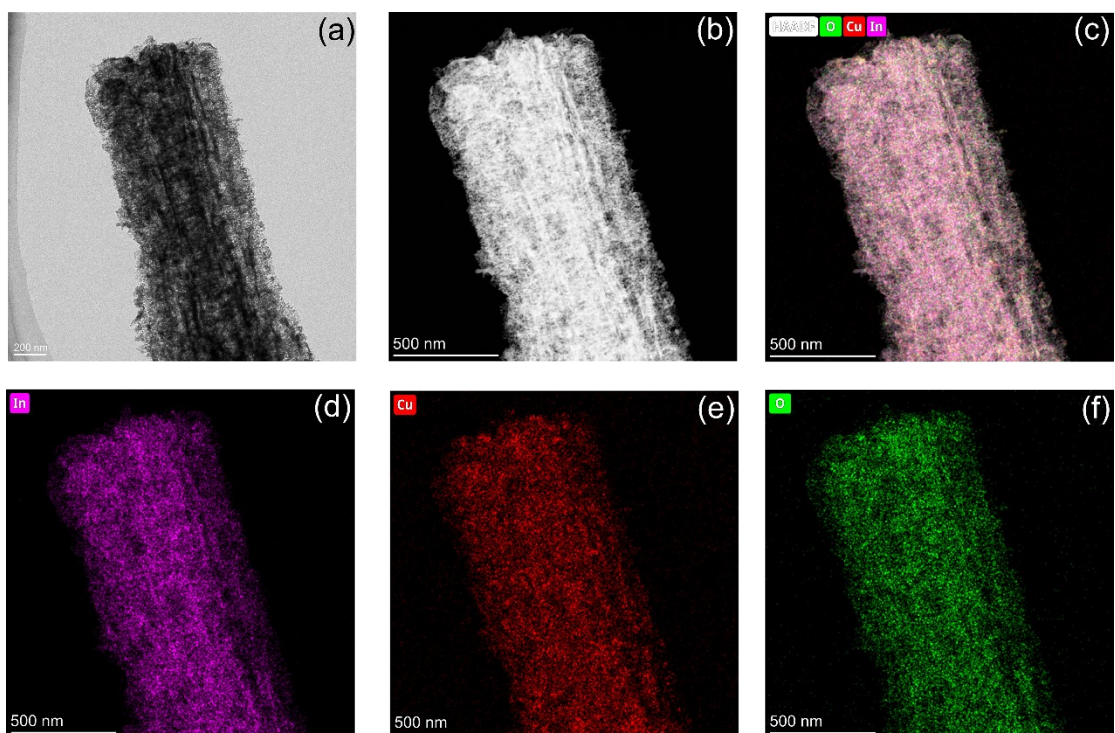
Figure S5. (a) TEM image, (b) HAADF and (c-f) elemental mapping by EDX of In$_2$O$_3$/Cu-O$_3$.
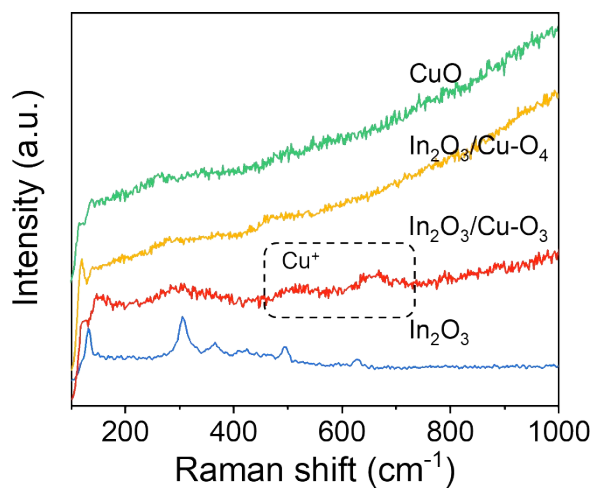
Figure S6. Raman spectra of In$_2$O$_3$, In$_2$O$_3$/Cu-O$_3$, In$_2$O$_3$/Cu-O$_4$ and CuO.
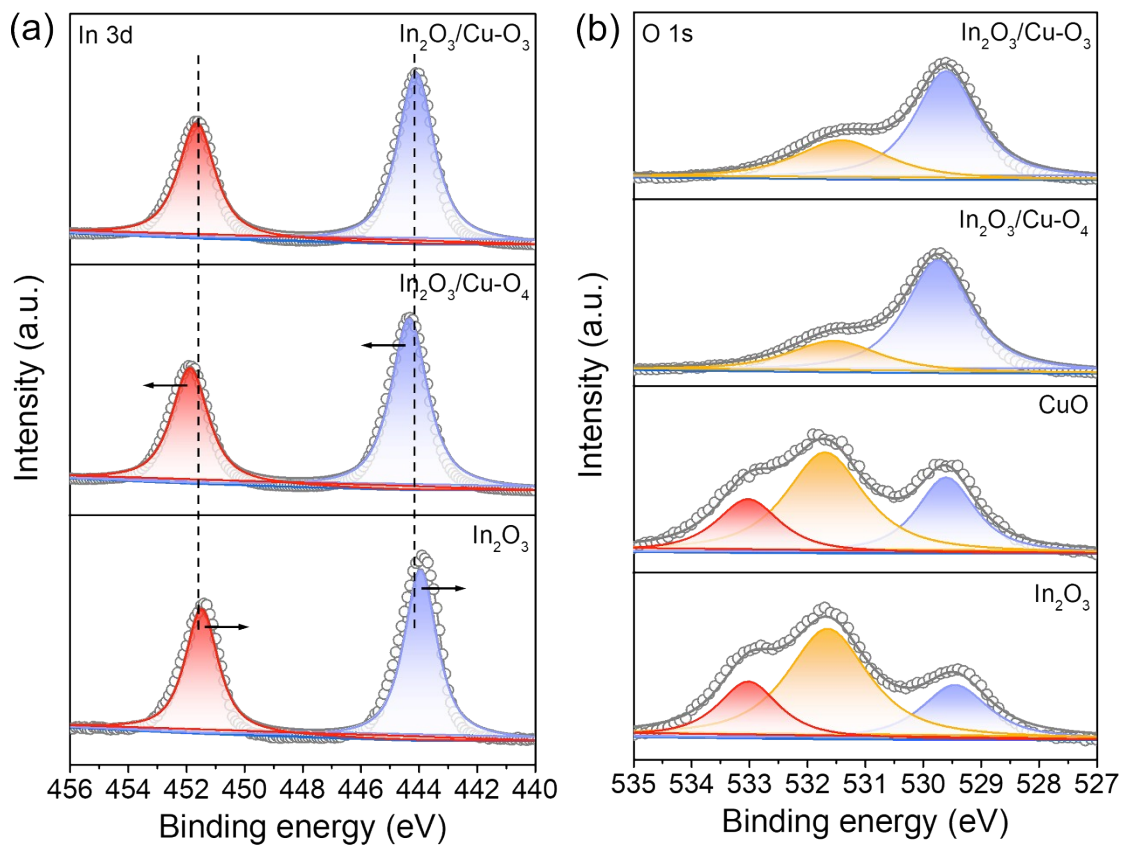
Figure S7. (a) In 3d XPS spectra of In_2O_3, $In_2O_3/Cu-O_3$ and $In_2O_3/Cu-O_4$. (b) O 1s XPS spectra of In_2O_3, $In_2O_3/Cu-O_3$, $In_2O_3/Cu-O_4$ and CuO.
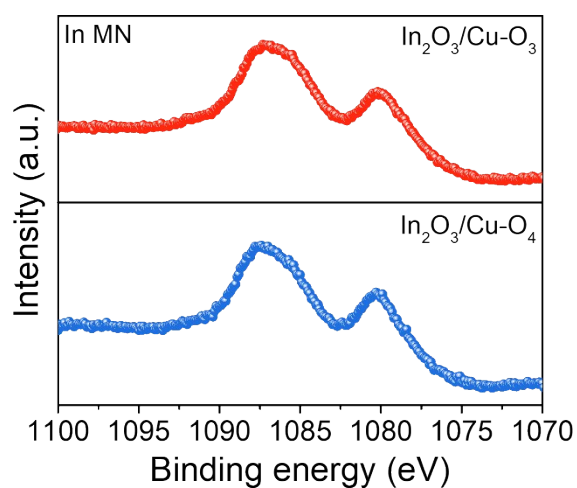
Figure S8. In MN AES spectra of $In_2O_3/Cu-O_3$ and $In_2O_3/Cu-O_4$.
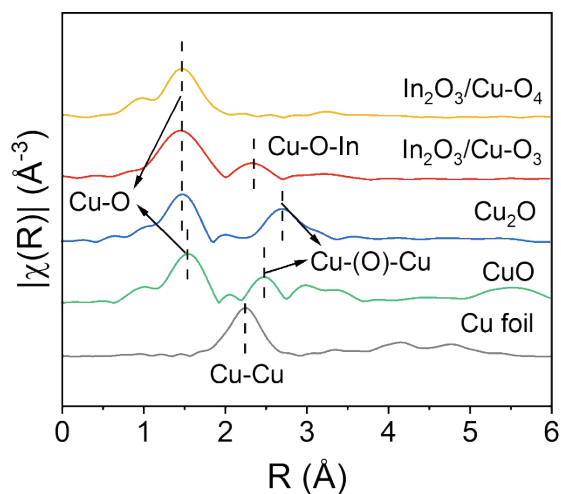
Figure S9. Fourier-transform of k^2-weighted EXAFS curves of Cu foil, Cu_2O, CuO, In_2O_3/Cu-O_3 and In_2O_3/Cu-O_4 in R spaces.
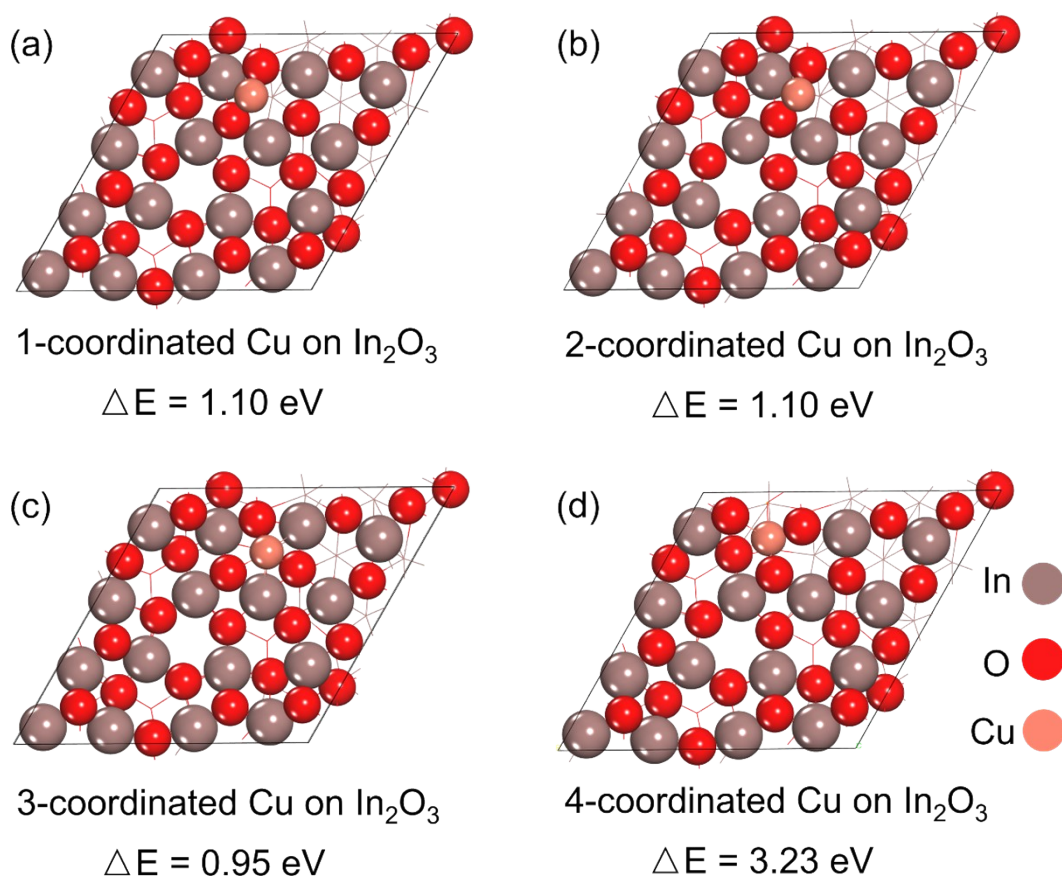
Figure S10. Structures and stability energies of different CNs of Cu on In_2O_3 (flesh-pink: In; red: O; light-red: Cu).
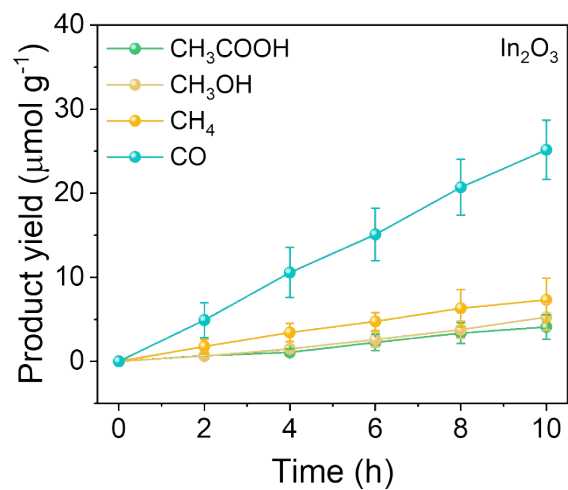
Figure S11. Photocatalytic CO$_2$RR property over In$_2$O$_3$.
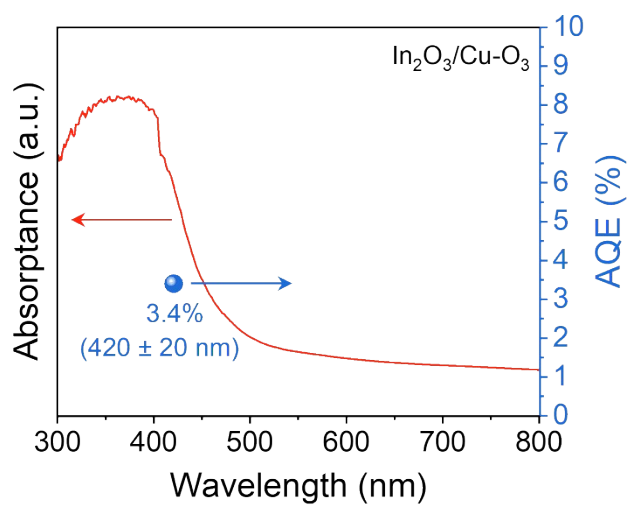
Figure S12. The AQE for ethanol production at In$_2$O$_3$/Cu-O$_3$ at 420 ± 20 nm.
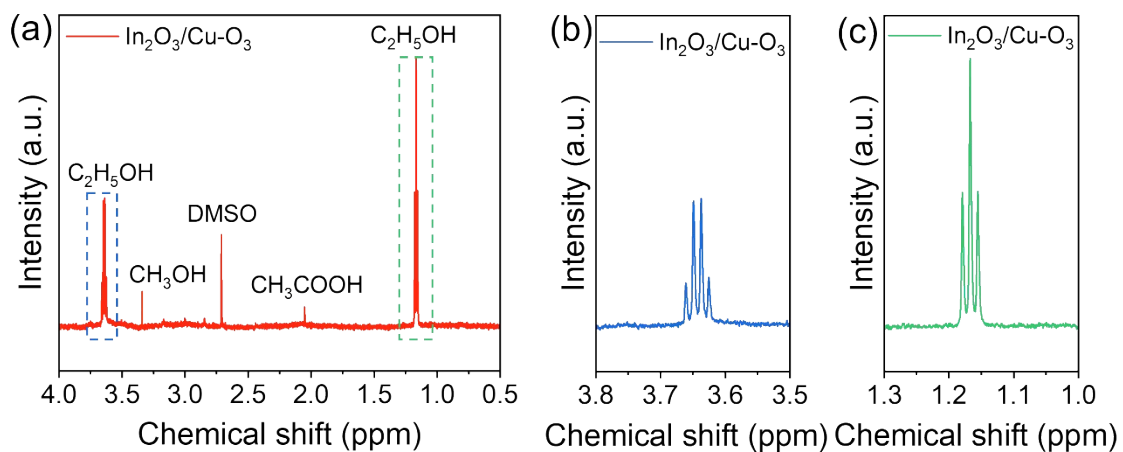
Figure S13. (a) ^1H NMR spectra for photocatalytic CO_2RR products over In_2O_3/Cu-O_3. The enlarged part of (b) the blue dashed box and (c) the green dashed box in (a).
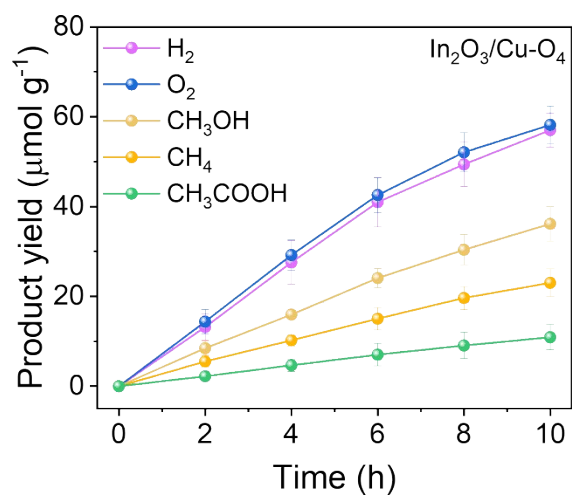
Figure S14. Photocatalytic CO_2RR property over In_2O_3/Cu-O_4.
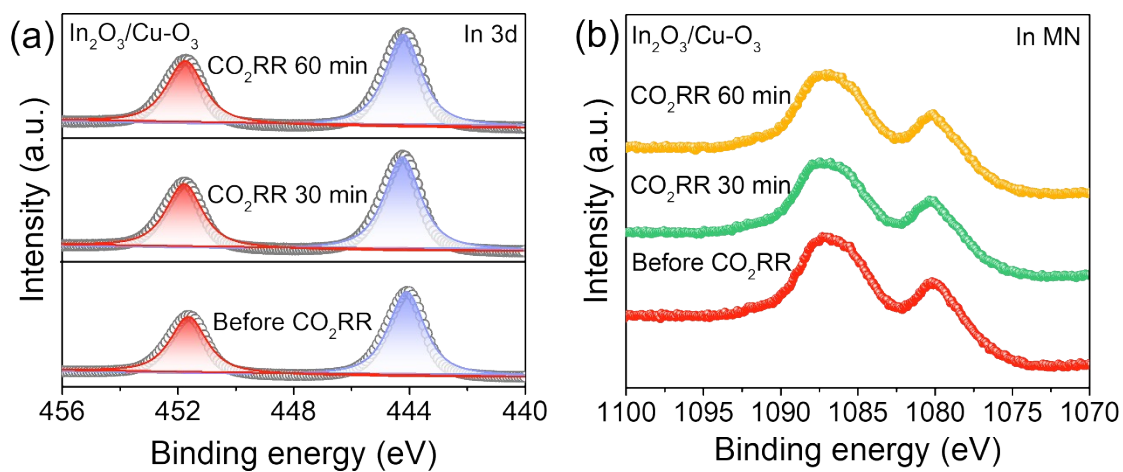
Figure S15. Quasi-in-situ (a) In 3d XPS and (b) In MN AES spectra of In_2O_3/Cu-O_3.
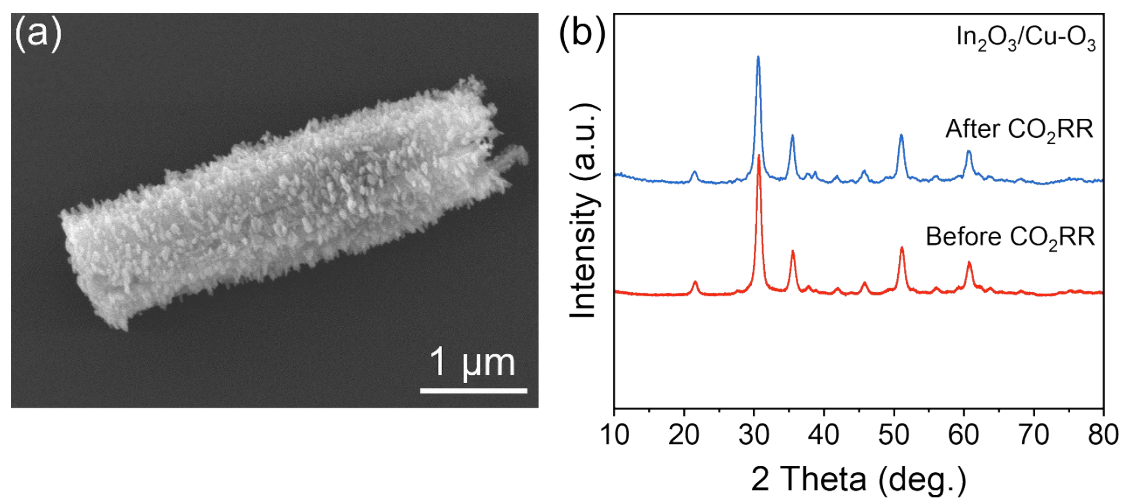
Figure S16. (a) SEM image and (b) XRD pattern of In_2O_3/Cu-O_3 after photocatalytic CO_2RR.
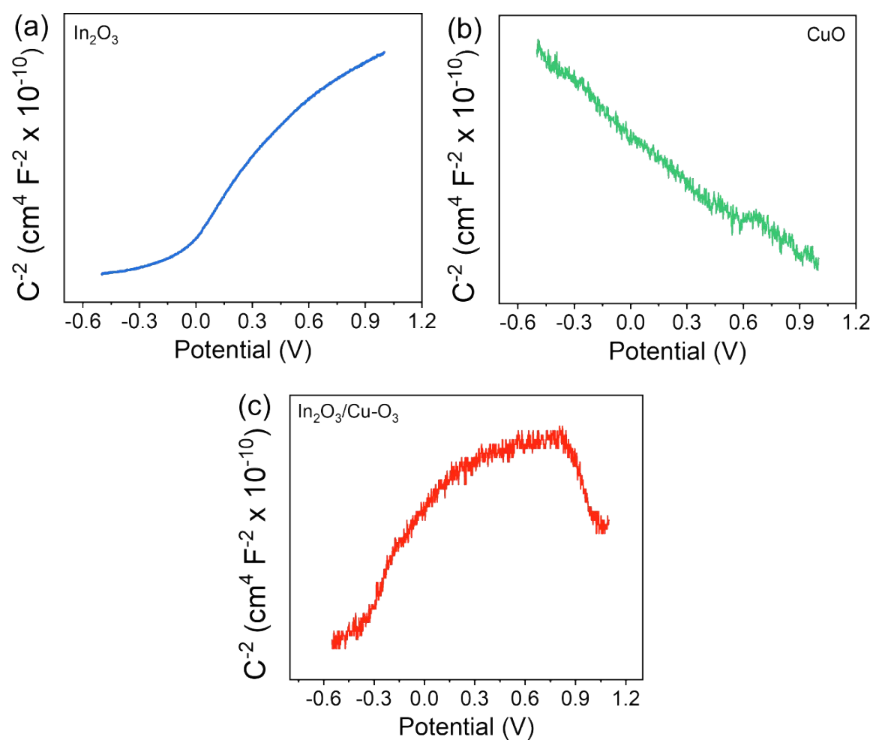
Figure S17. Mott–Schottky curves of (a) In_2O_3, (b) CuO, and (c) $In_2O_3/Cu\text{-}O_3$.
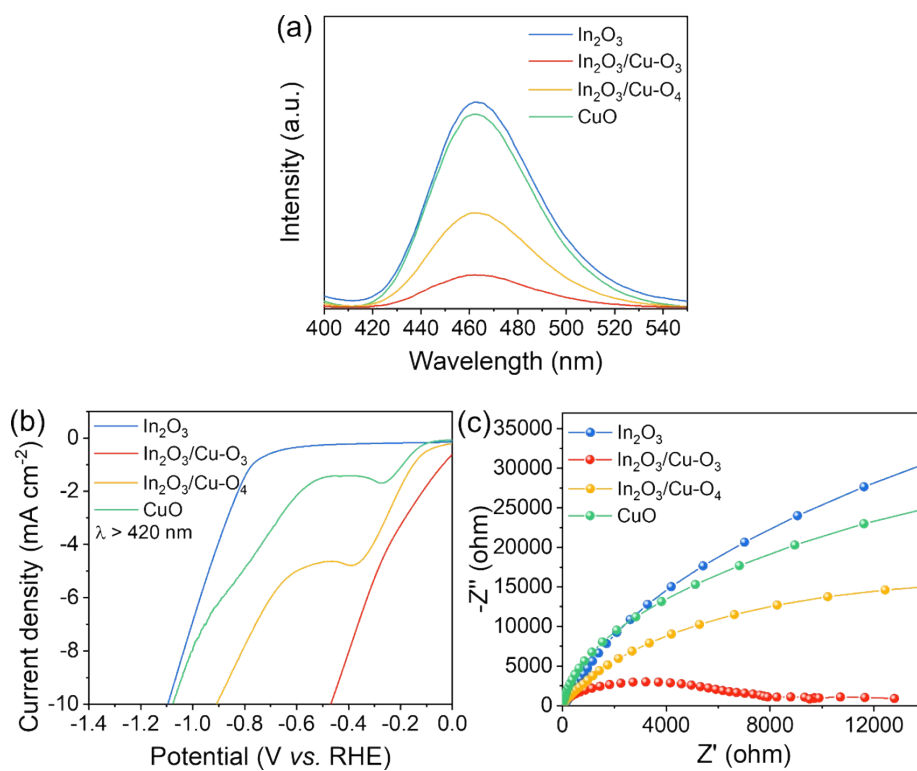
Figure S18. (a) PL spectra, (b) LSV curves, and (c) EIS of In_2O_3, $In_2O_3/Cu\text{-}O_3$,

In$_2$O$_3$/Cu-O$_4$ and CuO. LSV and EIS tests were performed in 0.5 M KHCO$_3$ saturated with CO$_2$ under visible light irradiation.
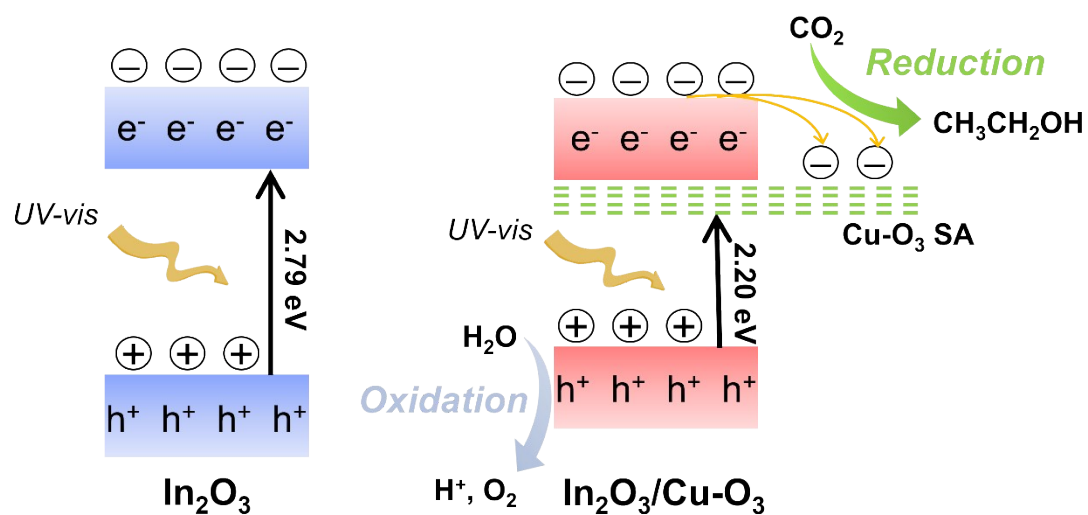
Figure S19. Schematic diagram of electron-hole transfer mechanisms on In$_2$O$_3$ and In$_2$O$_3$/Cu-O$_3$.
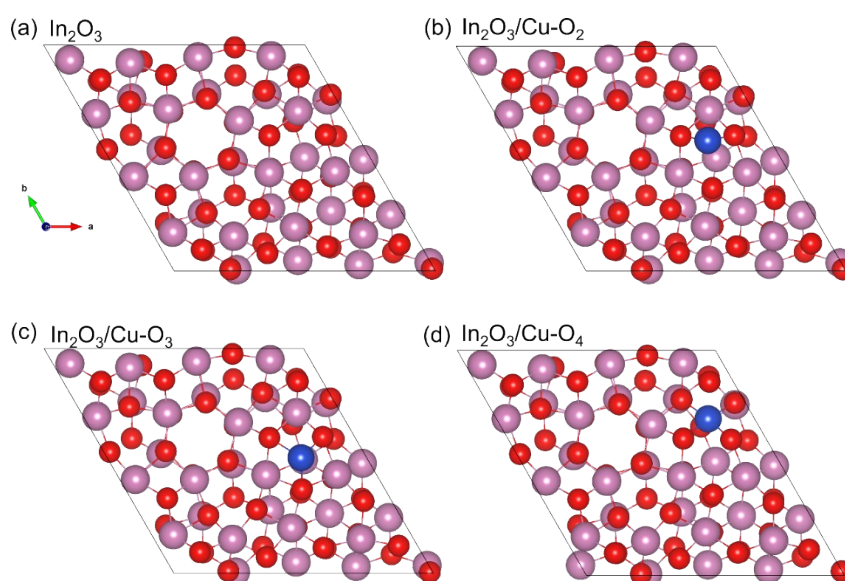
Figure S20. Calculated model slabs: (a) In$_2$O$_3$, (b) In$_2$O$_3$/Cu-O$_2$, (c) In$_2$O$_3$/Cu-O$_3$, and

(d) In$_2$O$_3$/Cu-O$_4$.

In$_2$O$_3$-*CO   In$_2$O$_3$-CO (g)
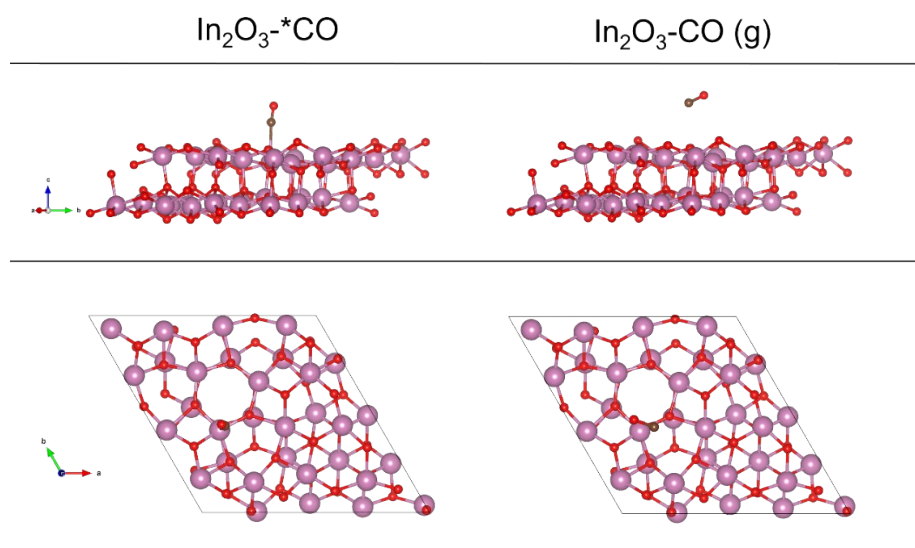
Figure S21. Calculated models of *CO and CO (g) adsorbed on In$_2$O$_3$.

In$_2$O$_3$-*COH   In$_2$O$_3$-*OCCOH   In$_2$O$_3$-*OCCO
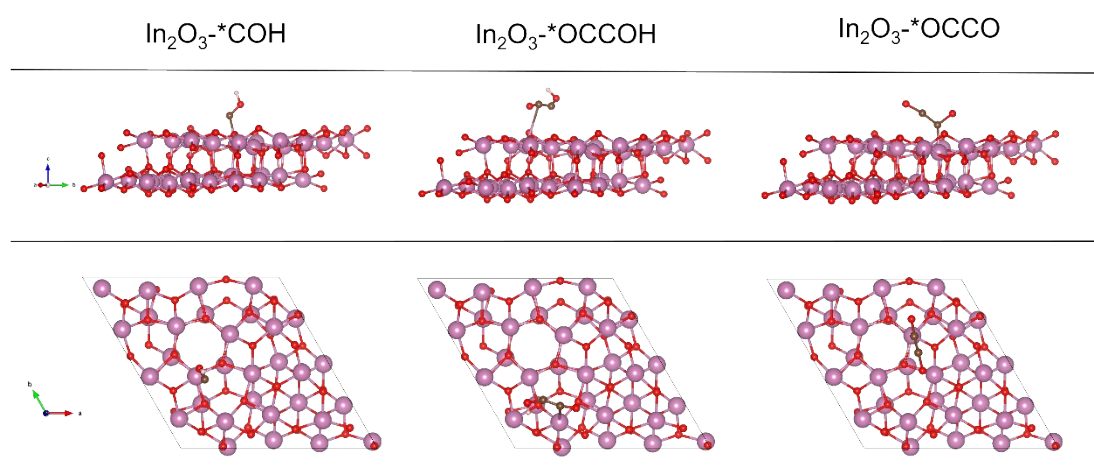
Figure S22. The models of intermediates adsorbed on In$_2$O$_3$.

In₂O₃/Cu-O₂-*CO   In₂O₃/Cu-O₂-*COH   In₂O₃/Cu-O₂-*OCCOH
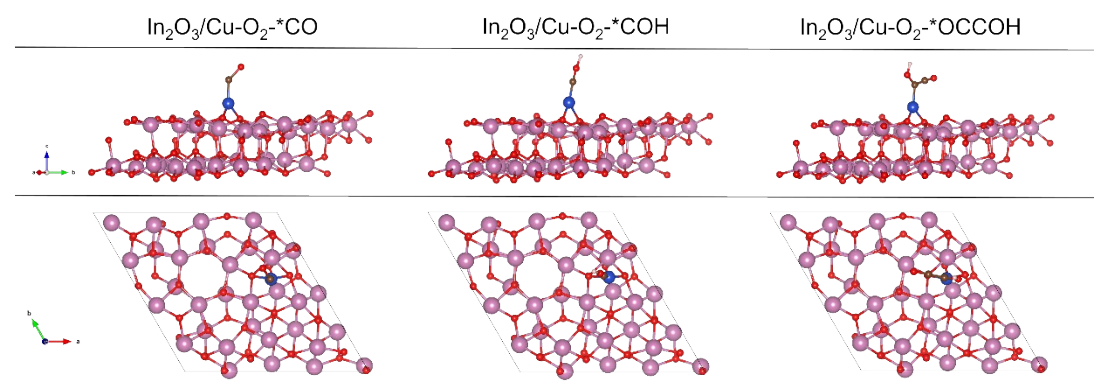
Figure S23. The models of intermediates adsorbed on In_2O_3/Cu-O_2.

In₂O₃/Cu-O₃-*CO   In₂O₃/Cu-O₃-*COH   In₂O₃/Cu-O₃-*CH₃
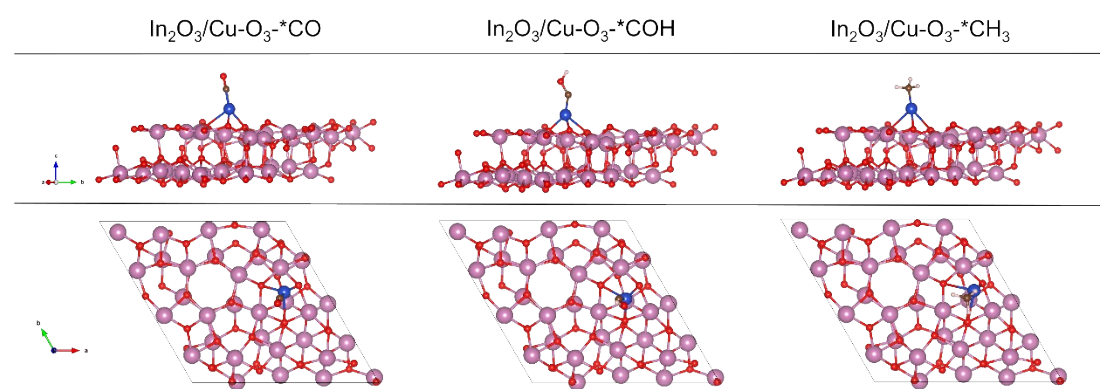
Figure S24. The models of intermediates adsorbed on In_2O_3/Cu-O_3.

In₂O₃/Cu-O₄-*CO   In₂O₃/Cu-O₄-*COH   In₂O₃/Cu-O₄-*OCCOH
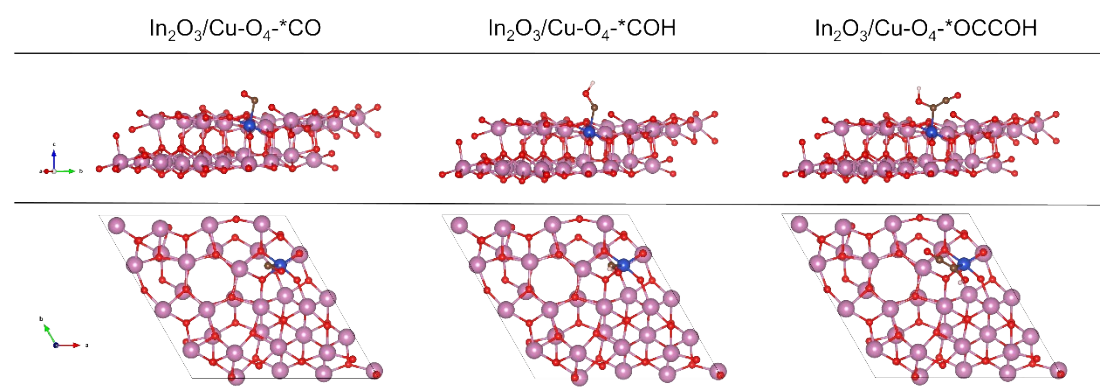
Figure S25. The models of intermediates adsorbed on In_2O_3/Cu-O_4.
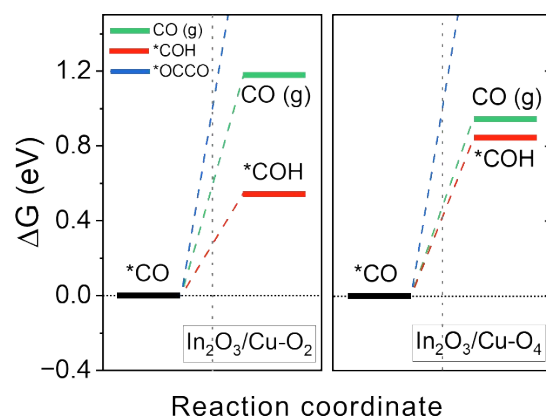
Figure S26. Free energy diagram on $In_2O_3/Cu-O_2$ and $In_2O_3/Cu-O_4$ of different pathways starting from *CO.
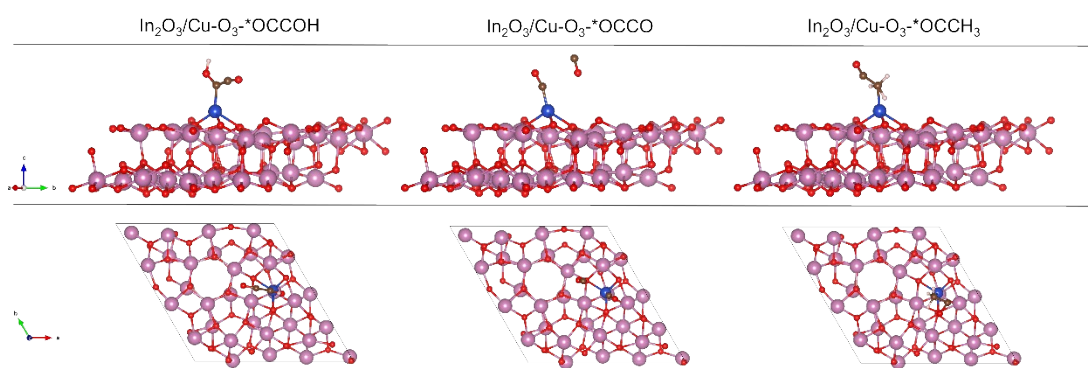
Figure S27. The models of C−C coupling intermediates adsorbed on $In_2O_3/Cu-O_3$.
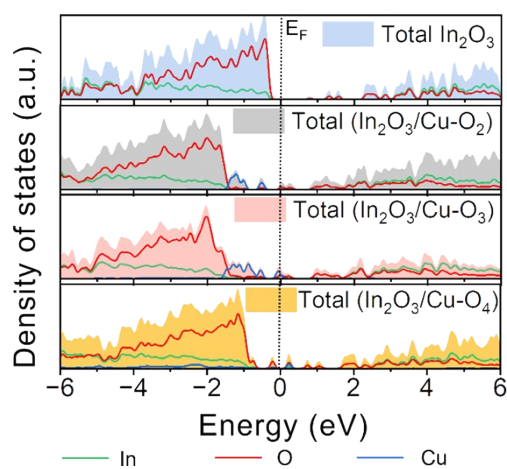
Figure S28. TDOS and LDOS of $In_2O_3/Cu-O_2$, $In_2O_3/Cu-O_3$ and $In_2O_3/Cu-O_4$.
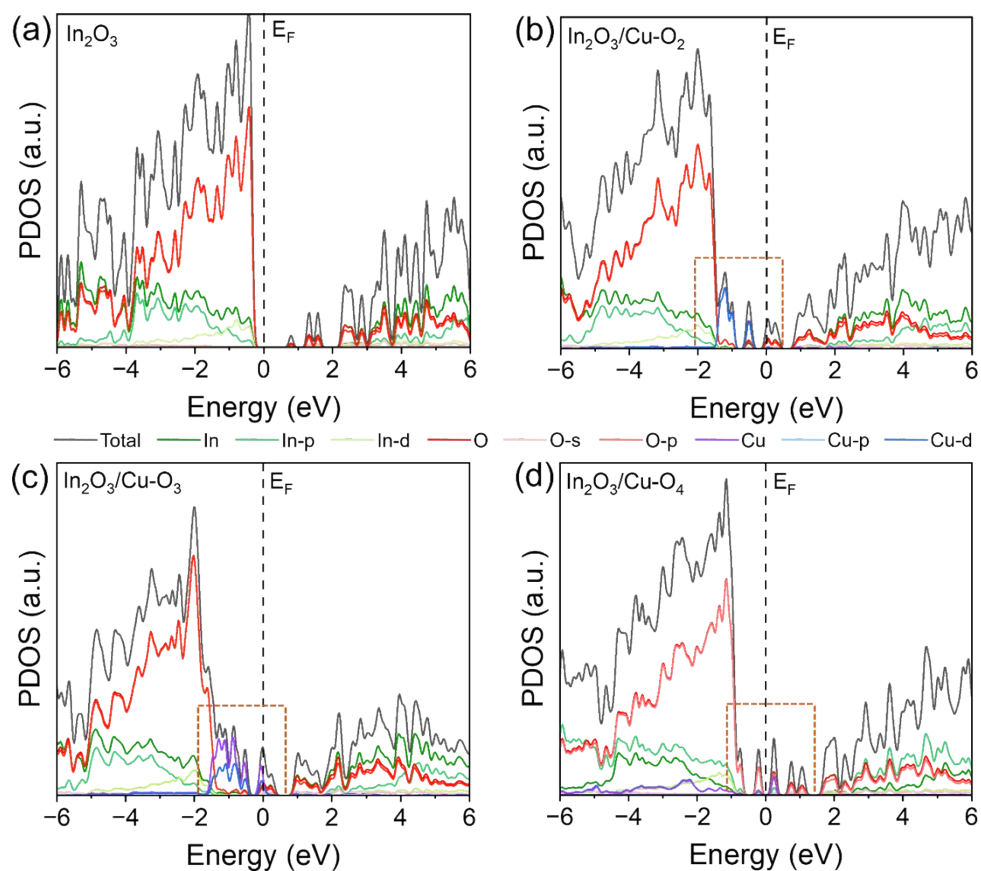
Figure S29. PDOS of (a) In$_2$O$_3$, (b) In$_2$O$_3$/Cu-O$_2$, (c) In$_2$O$_3$/Cu-O$_3$ and (d) In$_2$O$_3$/Cu-O$_4$.
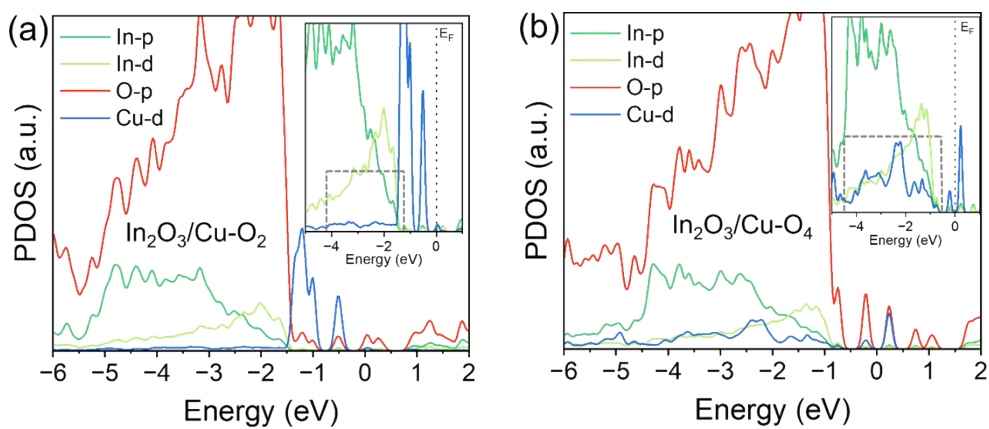
Figure S30. PDOS of (a) In$_2$O$_3$/Cu-O$_2$ and (b) In$_2$O$_3$/Cu-O$_4$.
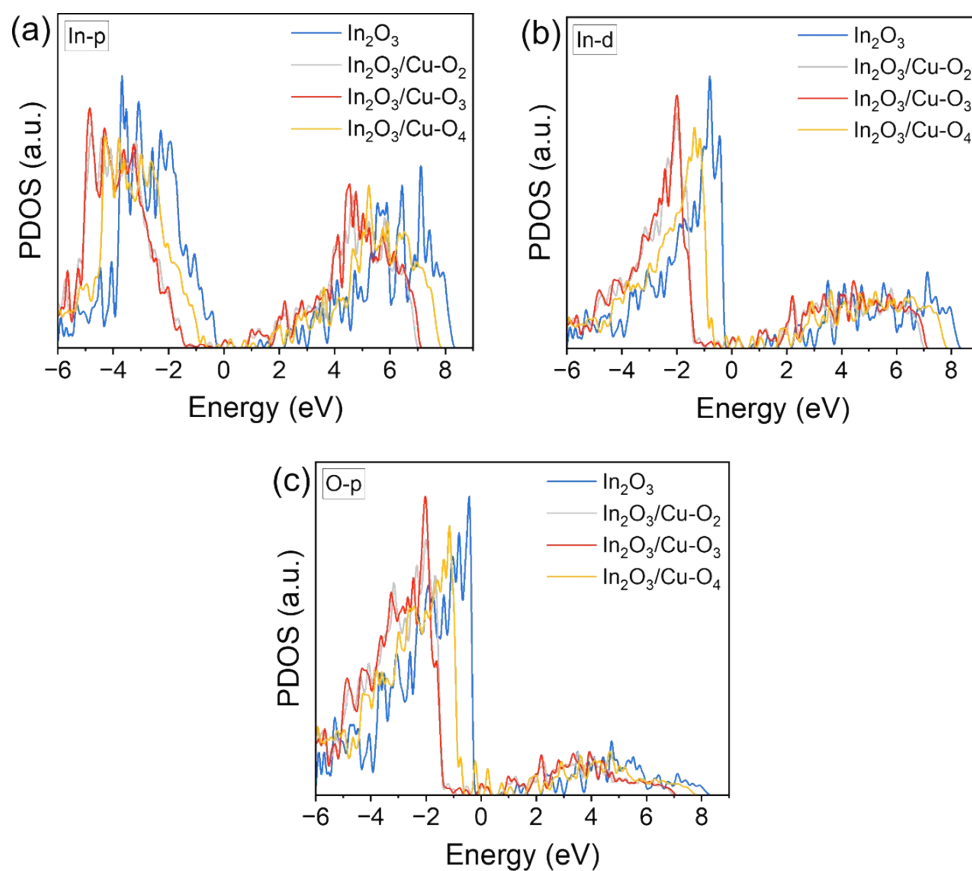
Figure S31. PDOS on In_2O_3, $In_2O_3/Cu-O_2$, $In_2O_3/Cu-O_3$ and $In_2O_3/Cu-O_4$ of (a) In p,

(b) In d and (c) O p orbitals.
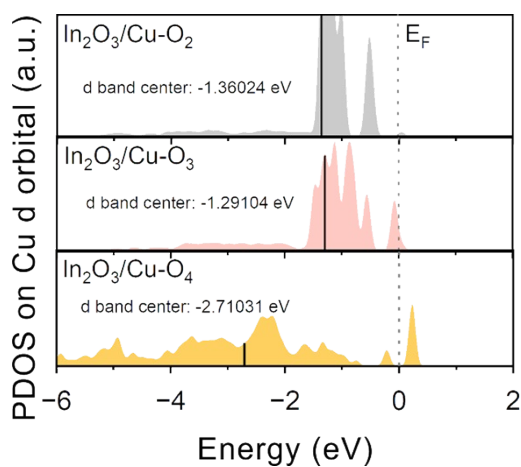
Figure S32. d band center of Cu on $In_2O_3/Cu-O_2$, $In_2O_3/Cu-O_3$ and $In_2O_3/Cu-O_4$.
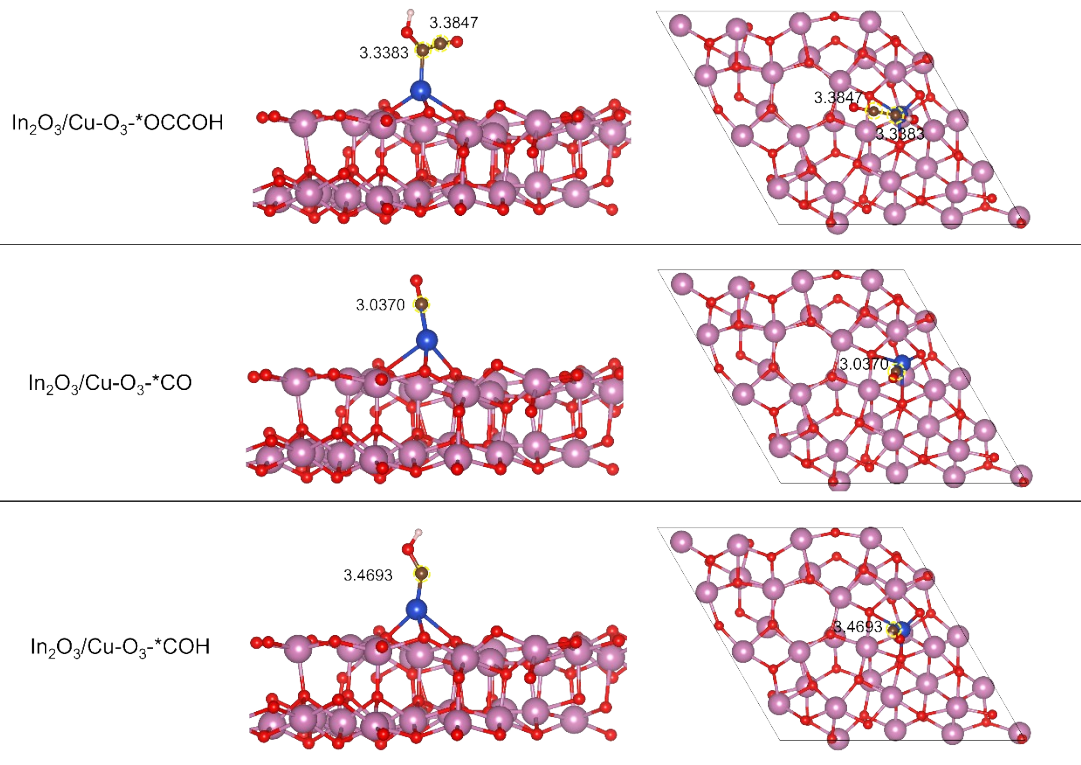
Figure S33. The Bader charge of carbon atoms of the adsorbed intermediates on In₂O₃/Cu-O₃.
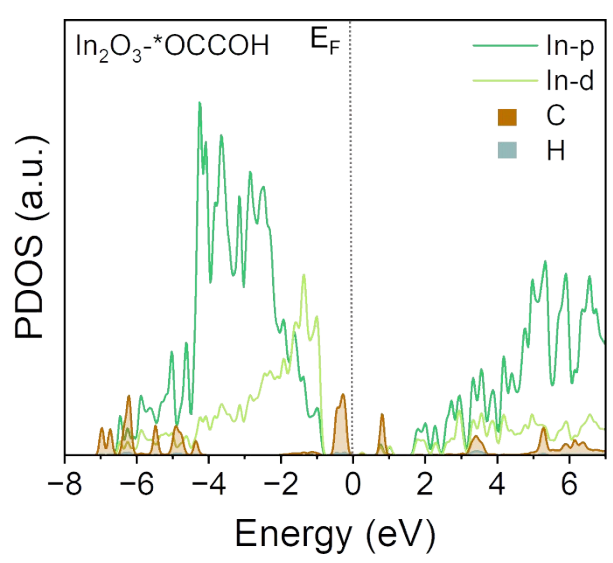
Figure S34. PDOS of In₂O₃ with *OCCOH intermediate adsorbed.
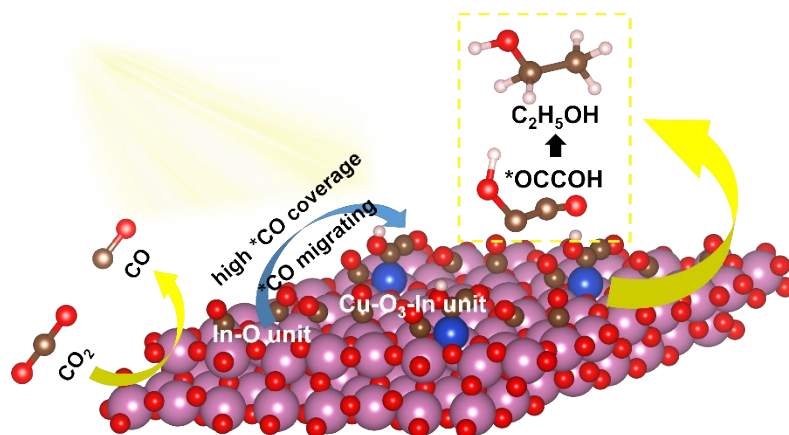
Scheme S1. Schematic representation of the mechanism for photoreduction of CO_2 to ethanol on $In_2O_3/Cu-O_3$.

Table S1. Actual loading content of Cu in In_2O_3/Cu-O_3 and In_2O_3/Cu-O_4 measured by ICP-OES.

Samples	Cu loading content (wt%)
In_2O_3/Cu-O_3	7.35
In_2O_3/Cu-O_4	13.41

Table S2. Curve fit parameters[a] for Cu K-edge EXAFS.

	shell	CN[b]	R (Å)[c]	σ^2 ($*10^{-3}$ Å^2)[d]	R factor
Cu foil	Cu−Cu	12 (set)	2.54 ± 0.003	8.73	0.005
CuO	Cu−O	1.04 ± 0.15	1.95 ± 0.013	4.05	0.017
	Cu−(O)−Cu	3.06 ± 0.77	2.93 ± 0.035		
Cu_2O	Cu−O	0.58 ± 0.09	1.86 ± 0.008	4.12	0.004
	Cu−(O)−Cu	1.73 ± 0.49	3.02 ± 0.023		
In_2O_3/Cu-O_3	Cu−O	1.02 ± 0.06	1.98 ± 0.010	4.92	0.003
	Cu−O−In	2.18 ± 0.25	2.63 ± 0.014		
In_2O_3/Cu-O_4	Cu−O	3.80 ± 0.29	1.95 ± 0.005	3.94	0.012

[a] S_0^2 was fixed as 0.85. ΔE_0 was refined as a global fit parameter, returning a value of (−3 ± 1 eV). Data ranges: $3.0 \le k \le 12.0$ Å^{-1}, $1.0 \le R \le 3.0$ Å. The number of variable parameters for sample is 4, out of a total of 9.47 independent data point.

[b] Coordination numbers; [c] Bonding distance; [d] Debye-Waller factor.

Table S3. Comparison of various photocatalysts for CO_2 photoreduction to ethanol.

Photocatalyst	Light source	Reaction medium	C_{2+} products	Production rate ($\mu mol\ g^{-1}\ h^{-1}$)	Selectivity	Ref.
InCu/PCN	300 W Xe	DMF/H_2O	C_2H_5OH	28.5	92.4%	[7]
BP-Bi_2MoO_6	450 W Xe	H_2O	C_2H_5OH	51.8	45.8%	[8]
TiO_2 {100}	UV-enhanced Xe (300 W)	0.1 M $NaHCO_3$	C_2H_5OH	6.2	66.7%	[9]
Cu SAs/UiO-66-NH_2	$\lambda > 400$ nm	TEOA/H_2O	C_2H_5OH	4.2	44.2%	[10]
Bi@Bi_2MoO_6	UV-enhanced Xe (300 W)	0.17 M $NaHCO_3$	C_2H_5OH	17.9	92.0%	[11]
NiZrCu-BDC	300 W Xe	acetonitrile/H_2O	C_2H_5OH	36.6	41.1%	[12]
$Bi_{19}S_{27}Cl_3$	20CGA-400 nm (420 W)	Na_2S/Na_2SO_3/H_2O	C_2H_5OH	5.2	85.0%	[13]
STO/Cu @ Ni/TiN	300 W Xe	H_2O	C_2H_5OH	21.3	79.0%	[14]
In_2O_3/Cu-O_3	**$\lambda > 420$ nm (300 W)**	**H_2O**	**C_2H_5OH**	**20.7**	**85.8%**	**This work**

Table S4. Bader charge of Cu atom on different models.

Sample	$In_2O_3/Cu-O_2$	$In_2O_3/Cu-O_3$	$In_2O_3/Cu-O_4$
Cu Bader (e^-)	0.6465	0.6596	1.1500

Table S5. Charge transfer from the slab to *CO according to Bader analysis.

Sample	In_2O_3	$In_2O_3/Cu-O_2$	$In_2O_3/Cu-O_3$	$In_2O_3/Cu-O_4$
Charge transfer (Δq_{*CO})	-0.0196	0.0688	0.0769	0.0107

Supplementary references

[1] B. Ravel, M. Newville, *J Synchrotron Radiat* **2005**, 12, 537.

[2] S. Gong, Y. Niu, X. Liu, C. Xu, C. Chen, T. J. Meyer, Z. Chen, *ACS Nano* **2023**, 17, 4922.

[3] G. Kresse, J. Furthmüller, *Phys Rev B* **1996**, 54, 11169.

[4] G. Kresse, D. Joubert, *Phys Rev B* **1999**, 59, 1758.

[5] P. E. Blöchl, *Phys Rev B Condens Matter* **1994**, 50, 17953.

[6] J. P. Perdew, K. Burke, M. Ernzerhof, *Phys Rev Lett* **1996**, 77, 3865−3868.

[7] H. Shi, H. Wang, Y. Zhou, J. Li, P. Zhai, X. Li, G. G. Gurzadyan, J. Hou, H. Yang, X. Guo, *Angew Chem Int Ed* **2022**, 61, 202208904.

[8] R. Das, K. Das, B. Ray, C. P. Vinod, S. C. Peter, *Energy Environmen Sci* **2022**,

15, 1967.

[9] M. P. Jiang, K. K. Huang, J. H. Liu, D. Wang, Y. Wang, X. Wang, Z. D. Li, X. Y. Wang, Z. B. Geng, X. Y. Hou, S. H. Feng, *Chem* **2020**, 6, 2335.

[10] G. Wang, C. T. He, R. Huang, J. Mao, D. Wang, Y. Li, *J Am Chem Soc* **2020**, 142, 19339.

[11] D. Zhao, Y. Xuan, K. Zhang, X. Liu, *ChemSusChem* **2021**, 14, 3293.

[12] M. Hu, J. Liu, S. Song, W. Wang, J. Yao, Y. Gong, C. Li, H. Li, Y. Li, X. Yuan, Z. Fang, H. Xu, W. Song, Z. Li, *ACS Catal* **2022**, 12, 3238.

[13] K. Das, R. Das, M. Riyaz, A. Parui, D. Bagchi, A. K. Singh, A. K. Singh, C. P. Vinod, S. C. Peter, *Adv Mater* **2023**, 35, 2205994.

[14] H. Yu, C. Sun, Y. Xuan, K. Zhang, K. Chang, *Chem Eng J* **2022**, 430, 132940.